Research Square

Preprints are preliminary reports that have not undergone peer review.
They should not be considered conclusive, used to inform clinical practice,
or referenced by the media as validated information.

On the Flattening of the Inertial-Subrange Slope During the Afternoon Transition of the Convective Boundary Layer: A Spectral Turbulence Kinetic Energy Budget Analysis

Antonio Goulart

antonio.goulart@furg.br

Universidade Federal do Rio Grande

Matheus Jatkoske Lazo

Universidade Federal do Rio Grande

Julian Moises Sejje Suarez

Universidade Federal do Rio Grande

Research Article

Keywords: Afternoon transition, Convective boundary layer, Energy spectrum, Fractal dimension, Turbulence decay

Posted Date: August 4th, 2026

DOI: https://doi.org/10.21203/rs.3.rs-10499739/v1

License: This work is licensed under a Creative Commons Attribution 4.0 International License.
Read Full License

Additional Declarations: No competing interests reported.

Boundary-Layer Meteorology manuscript No.
(will be inserted by the editor)

On the Flattening of the Inertial-Subrange Slope During the Afternoon Transition of the Convective Boundary Layer: A Spectral Turbulence Kinetic Energy Budget Analysis

Antonio Goulart · Matheus Jatkoske Lazo · Julian Moises Sejje Suarez

Received: DD Month YEAR / Accepted: DD Month YEAR

Abstract
During the afternoon transition of the convective boundary layer (CBL), BLLAST observations and large-eddy simulation (LES) show that the inertial-subrange slope of the vertical-velocity spectrum flattens, and the spectral sharpness parameter collapses, during the last two hours before the surface heat flux vanishes, while near-surface spectra remain unchanged; under fully convective conditions the same spectra are steeper than the Kolmogorov prediction. This behaviour is investigated with a spectral model for the time evolution of the turbulence kinetic energy (TKE) spectrum, extended in three directions: (i) the initial spectrum is built from the complete anisotropic spectral velocity tensor of Kristensen et al. and made an exact stationary solution of the discrete spectral balance, fixing all closure constants without empirical adjustment; (ii) the inertial transfer is generalized to an intermittent (beta-model) cascade of fractal dimension smaller than unity, and the one-dimensional components through a transition-sharpness parameter, with static vertical profiles of both parameters calibrated once on the midday slopes and afternoon sharpness plateaus of the LES (fractal dimensions of 0.60 to 0.81: markedly intermittent at every height); (iii) the thermal forcing is decomposed into surface, entrainment and penetrative-transport components with quadratic shut-off laws. The

A. Goulart
Institute of Mathematics, Statistics and Physics – IMEF, Universidade Federal do Rio Grande, 96201-900 Rio Grande, RS, Brazil
E-mail: antonio.goulart@furg.br

M. J. Lazo
Institute of Mathematics, Statistics and Physics – IMEF, Universidade Federal do Rio Grande, 96201-900 Rio Grande, RS, Brazil
E-mail: matheuslazo@furg.br

J. M. S. Suarez
Institute of Mathematics, Statistics and Physics – IMEF, Universidade Federal do Rio Grande, 96201-900 Rio Grande, RS, Brazil
E-mail: julian.sejje@furg.br

model reproduces the two-phase, nearly height-homogeneous TKE decay, the magnitude, vertical shape and stability of the sharpness plateau, the slope flattening and the surface invariance. The flattening emerges as the spectral-budget signature of the progressive shut-off of the distributed buoyant source over a fixed intermittent cascade geometry: no change of cascade efficiency or anisotropy is required; a sudden shut-off instead narrows the spectrum.

Keywords Afternoon transition · Convective boundary layer · Energy spectrum · Fractal dimension · Turbulence decay

1 Introduction

The decay of convective turbulence during the afternoon and evening transition is one of the less understood regimes of the atmospheric boundary layer. As the surface sensible heat flux weakens and changes sign, the convective boundary layer (CBL) loses its energy source over a time scale comparable to the turnover time of its largest eddies, and the turbulence it contains neither remains quasi-stationary nor decays freely: it decays while it is still, for a while, being forced. The regime matters practically—the transition controls the vertical dispersion of pollutants emitted in the late afternoon, sets the initial conditions of the nocturnal and residual layers, and challenges the surface-flux–based similarity closures used in weather and dispersion models (Nieuwstadt and Brost 1986; Sorbjan 1997; Pino et al. 2006; Nadeau et al. 2011; Rizza et al. 2013). It has been studied through large-eddy simulation (LES) since the pioneering shut-off experiments of Nieuwstadt and Brost (1986), through observations of the afternoon CBL (Grant 1997; Grimsdell and Angevine 2002), and, comprehensively, by the Boundary Layer Late Afternoon and Sunset Turbulence (BLLAST) field experiment (Lothon et al. 2014).

Nieuwstadt and Brost (1986) considered a sudden shut-off of the surface heat flux and found that the decay occurs within a period of the order of the convective time scale $t_* = z_i/w_*$, with evidence of a decoupling between large and small scales. Sorbjan (1997) considered instead a gradual decrease of the forcing, governed by an external time scale τ_f, and showed that when τ_f is large relative to t_* the turbulence adjusts quasi-statically to the changing forcing, the largest eddies decaying more slowly than the small ones; a decoupled residual layer of active turbulence develops above the stabilizing surface layer. Pino et al. (2006) examined systematically, by LES, the role of shear and of the inversion strength on the decay, finding an increase of the anisotropy in all cases and characteristic length scales that generally grow during the decay—except that of the vertical velocity, fixed by pressure correlations. Rizza et al. (2013) simulated the sunset decay under realistic (observed) forcing, and Nadeau et al. (2011) proposed a simple model for the near-surface TKE decay over different land surfaces. More recent LES studies have refined this picture. Park et al. (2020), spanning stability parameters $-z_i/L$ from 5.7 to 364, showed that after a sudden shut-off the boundary-layer-averaged TKE holds for about

one turnover time and then decays with an exponent ≈1.2 in the buoyancy-dominated cases, while wind shear delays—and can even arrest—the decay. El Guernaoui et al. (2019), prescribing gradual heat-flux decays of varying duration τ, found that the TKE evolution is dictated by the decaying flux up to $\approx 0.7\tau$ and that, once the time origin is redefined at the evening transition, the subsequent free decay exhibits a universal exponent close to unity, independent of τ and of the initial convective state. Tkachenko et al. (2022) distinguished a fast-decay interval of duration $\sim t_*$—dominated by the consumption of the vertical velocity component and by energy isotropization—from a slow-decay interval in which the anisotropy grows again and a quasi-two-dimensional flow forms, and showed that two-equation RANS closures fail to reproduce this two-interval structure; the sensitivity of the simulated decay rates to the subgrid closure and grid resolution has likewise been documented (Tkachenko et al. 2021). On the theoretical side, the spectral approach of Goulart et al. (2003, 2011) describes the decay through the dynamical equation for the three-dimensional energy-density spectrum, retaining the buoyant production, the mechanical production and the nonlinear inertial transfer, with closure constants fixed by the initial equilibrium; from the decaying spectrum, eddy diffusivities for dispersion models in the decaying CBL have been derived (Goulart et al. 2007; Goulart 2026), of interest for Eulerian air-quality models in the late afternoon (Koleva and Vulkov 2023).

Analysing the BLLAST case of 20 June 2011 with both aircraft observations and LES, Darbieu et al. (2015) documented a specific and, at first sight, counterintuitive spectral behaviour. (i) Under fully convective midday conditions, the inertial-subrange slope of the vertical-velocity spectrum is steeper than the Kolmogorov value ($-5/3$ in $S(k)$, $-2/3$ pre-multiplied), a feature also found by airborne Doppler lidar in other datasets (Lothon et al. 2009). (ii) Late in the transition the slope consistently flattens, the change starting at the top of the CBL around 1600 UTC and propagating downwards with decreasing amplitude. (iii) The sharpness parameter μ of the analytical spectral model of Kristensen et al. (1989) (hereafter KL89), fitted to the observed and simulated spectra, holds a plateau $\mu \simeq 2$ above $0.15\, z_i$ throughout the afternoon and collapses during the last two hours before the heat flux vanishes, while near the surface $\mu \simeq 0.5$ remains unchanged all day. (iv) To explain the flattening, Darbieu et al. (2015) advanced two hypotheses—an increase of anisotropy altering the energy cascade, or a more efficient cascade in free decay, in the spirit of Moeng and Wyngaard (1988)—but neither was tested quantitatively.

In this work, we employ the analytical spectral model of Goulart et al. (2011) to investigate the change in slope, because it retains—within a prognostic equation for the energy density spectrum—precisely those balance terms that can affect the inertial subrange (distributed thermal and mechanical production, nonlinear inertial transfer, and molecular dissipation), and because anisotropy enters through the initial three-dimensional spectrum.

This work aims, firstly, to reproduce the spectral evolution observed in the BLLAST case using the spectral model—specifically, the two-phase TKE

decay, the plateau and collapse of μ, the slope flattening, and the surface invariance. Secondly, it seeks to attribute this flattening to specific terms in the spectral budget through numerical "switch-on/switch-off" experiments—an approach not feasible with LES. Thirdly, it aims to explain the vertical structure of the transition—identifying which changes begin at the top and why the surface remains sheltered. To this end, we introduce three extensions to the model: an initial spectrum built from the complete (anisotropic) spectral velocity tensor of Kristensen et al. (1989), made an exact stationary solution of the discrete spectral balance by the closure of the transfer velocity; an intermittent (fractal) cascade with a height-dependent dimension, based on the β-model spectra developed by Goulart et al. (2022, 2024), together with a height-dependent sharpness of the one-dimensional components within the Kristensen spectral family; and a component-specific decay law for thermal forcing—with each of these extensions constrained by an independent dataset. The analysis is restricted to the convective window $t \leq \tau_f$: after the buoyancy-flux reversal the nascent residual layer is dominated by wave motions outside the domain of the convective spectral family (Sect. 5.2).

The paper is organized in the following way: In Sect. 2, the observational problem is stated quantitatively. In Sect. 3, the spectral model and its extensions are developed. The results are presented in Sect. 4 and discussed in Sect. 5, which also contains the physical interpretation and the limitations of the model. Section 6 presents the conclusions.

2 The Observational Problem

The BLLAST intensive observation period of 20 June 2011—a cloud-free, weak-wind day (mean wind $\sim 2\,\mathrm{m\,s^{-1}}$) over the Lannemezan plateau—is the reference case of this study, as well as for Darbieu et al. (2015). The surface buoyancy flux peaks near 1200 UTC and crosses zero at ≈1750 UTC, defining a forcing decay time $\tau_f \approx 21\,000$ s; the CBL depth is $z_i \approx 1100$–1400 m, the midday convective velocity $w_* \approx 1.5\,\mathrm{m\,s^{-1}}$, and the friction velocity decreases from ≈0.2 to $\approx 0.1\,\mathrm{m\,s^{-1}}$ during the afternoon. Because $\tau_f/t_* \approx 30$ (with $t_* = z_i/w_*$ the convective turnover time), the decay is slow in the sense of Sorbjan (1997): the turbulence adjusts quasi-statically during most of the afternoon. This regime assignment is supported independently by the free-convective LES of El Guernaoui et al. (2019), in which the TKE evolution is dictated by the decaying heat flux up to $\approx 0.7\tau$, with the convective scaling breaking down around 0.8τ—in agreement with the two-phase separation at $0.75\,\tau_f$ of Darbieu et al. (2015) adopted below—and by the weak wind of the case, which places it in the buoyancy-dominated class of the shear-sensitivity study of Park et al. (2020).

The findings of Darbieu et al. (2015) define five quantitative targets for the model.

1. **Two-phase TKE decay.** The TKE decays slowly until $\sim 0.75\,\tau_f$, preserving its convective characteristics, and rapidly afterwards; the relative decay is nearly homogeneous in height.
2. **Onset times.** By an absolute-rate criterion, the TKE decay starts near 1300 UTC, with a slight tendency to start earlier at the top.
3. **Slope flattening.** The pre-multiplied inertial-subrange slope of the vertical-velocity spectrum, steeper than $-2/3$ at midday, flattens after ≈1600 UTC in the upper CBL and after ≈1745 UTC at $0.15\,z_i$.
4. **μ plateau and collapse.** The KL89 sharpness parameter holds $\mu \simeq 2$–2.5 above $0.15\,z_i$ (with a maximum at 0.45–$0.6\,z_i$) until ≈1600 UTC and collapses to $\lesssim 1$ by 1830 UTC; near the surface $\mu \simeq 0.5$ is invariant.
5. **Length scales.** The peak wavelength Λ_w ($\simeq 1.5\,z_i$ at midday at mid-CBL) shifts to smaller wavelengths late in the transition.

3 The Spectral Model

3.1 Budget Equation for the Energy-Density Spectrum

Following Goulart et al. (2003, 2011), the three-dimensional energy-density spectrum $E(k,t,z)$ at each height z evolves according to

$$\frac{\partial E(k,t,z)}{\partial t} = M(k,t,z) + W(k,t,z) + \frac{g}{T_0} H(k,t,z) - 2\nu k^2 E(k,t,z), \qquad (1)$$

where M is the mechanical (shear) production, W the inertial transfer, $(g/T_0)H$ the buoyant production and the last term the molecular dissipation. The inertial transfer is written in flux form,

$$W(k,t,z) = -\frac{\partial}{\partial k}\Big[v(k,t)\,E(k,t,z)\Big], \qquad v(k,t) = \Big(\frac{\varepsilon_{\rm eff}(t)}{\varepsilon_0}\Big)^{1/3} v_{\rm st}(k), \qquad (2)$$

where v is the spectral flux velocity, $\varepsilon_{\rm eff}(t)$ is the effective dissipation rate, computed self-consistently from the evolving spectrum (defined at the end of this subsection), and $\varepsilon_0 = \varepsilon_{\rm eff}(0)$ is its initial (midday) value. In Goulart et al. (2003, 2011) v was specified by the closure of Pao (1965), $v = \alpha^{-1}\varepsilon^{1/3}k^{5/3}$ with $\alpha = 1.5$ the Kolmogorov constant, supplemented by the high-wavenumber correction of Frisch (1995) (a separate closure constant c_2). Here, instead, the stationary velocity $v_{\rm st}$ is determined by the initial balance itself,

$$v_{\rm st}(k) = \frac{\Phi(k)}{E_0(k)}, \qquad \Phi(k) = \int_0^k \Big[S_H(k',0) + S_M(k',0) - 2\nu k'^2 E_0(k')\Big]\,dk', \quad (3)$$

where S_H and S_M are the buoyant and mechanical sources defined below: Eq. 3 is the unique flux velocity for which the initial spectrum E_0 is an *exact* stationary solution of Eq. 1 at $t = 0$ (Φ is computed with the same discrete upwind operator as the time integrator, so that E_0 is an exact fixed point of the numerical scheme; $\Phi(k) > 0$ at all k). The temporal modulation $(\varepsilon_{\rm eff}/\varepsilon_0)^{1/3}$ preserves

the Pao scaling of the flux velocity with the dissipation rate. For space-filling isotropic equilibrium turbulence $v_{\rm st}$ recovers the Pao form $\alpha^{-1}\varepsilon^{1/3}k^{5/3}$, and its high-wavenumber limit reproduces the fractal generalization of Sect. 3.2; the Frisch correction is absorbed into $v_{\rm st}$ and no longer exists as a separate constant. The buoyant source is factorized into its initial spectral shape and a prescribed decay of the surface forcing (Sorbjan 1997),

$$\frac{g}{T_0}H(k,t,z) = c_1\,\frac{w_*^3}{(\overline{w\theta})_0\,z_i}\,\varepsilon^{-1/3}k^{-2/3}E_0(k,z)\,S_H(t,z), \tag{4}$$

where $(\overline{w\theta})_0$ is the surface kinematic heat flux, $w_* = [(g/T_0)(\overline{w\theta})_0\,z_i]^{1/3}$ the convective velocity scale, z_i the CBL depth and ε the local dissipation rate, obtained from the dimensionless rate of Eq. 6 below. The spectral weight $k^{-2/3}E_0$ distributes the production over wavenumbers—including the low-wavenumber edge of the inertial subrange—and the vertical and temporal structure of S_H is specified in Sect. 3.4. The mechanical term follows Monin–Obukhov similarity,

$$M(k,t,z) = c_m\,\frac{\phi_m\,\phi_\varepsilon^{-1/3}\,u_*^2(t)}{(\kappa z)^{2/3}}\,k^{-2/3}E_0(k,z), \tag{5}$$

where ϕ_m and ϕ_ε are the Monin–Obukhov similarity functions for the wind shear and for the dissipation rate, u_* is the friction velocity and $\kappa = 0.4$ the von Kármán constant, with $u_*(t)$ decreasing from 0.2 to 0.1 $\mathrm{m\,s^{-1}}$ as observed. The closure constant c_1 is determined, as before, by the initial equilibrium (Eq. 7 of Goulart et al. 2003), and the transfer velocity by Eq. 3; no constant of the model is tuned to the decay data. The dissipation rate is computed self-consistently from the evolving spectrum, $\varepsilon_{\rm eff} = \varepsilon_0\,(\mathrm{TKE}/\mathrm{TKE}_0)^{3/2}\,(l_0/l)$ with $l = \int (E/k)\,dk \big/ \int E\,dk$.

The system is solved by the method of lines on a logarithmic wavenumber grid (400 points), with a conservative upwind discretization of the transfer term and a backward-differentiation time integrator. Because E_0 is an exact fixed point of the discrete balance, no spin-up is required: the numerical initial state is the stationary solution itself, and the one-dimensional components effectively used are exactly those prescribed below.

For the initial spectrum $E_0(k,z)$ and its one-dimensional components we adopt the convective spectra of Goulart et al. (2024) with the dimensionless dissipation rate

$$\psi_\varepsilon = 0.62\,(z/z_i)^{-1/3}(1 - z/z_i)^{1/4}, \tag{6}$$

an LES-based adjustment. This dimensionless dissipation rate yields an initial TKE profile decreasing monotonically with height (Fig. 1c) and, together with the stationary closure of Eq. 3, an initial state in exact spectral-budget equilibrium.

The three-dimensional initial spectrum is obtained from the one-dimensional component spectra through the complete spectral velocity tensor of KL89

(their Eq. 52),

$$E_0(k,z) = k^3\,\frac{\partial}{\partial k}\left[\frac{1}{k}\,\frac{\partial F_u(k,z)}{\partial k}\right] + 2k^4\int_0^{1/k^2} s^2\,g'''(s)\,ds - \frac{14}{9}\,k^{4/3}\int_0^{1/k^2} s^{2/3}\,g'''(s)\,ds, \tag{7}$$

where $g(s) = J(s^{-1/2})\,s^2$ and

$$J(k) = F_u(k) - k\,F_u'(k) - \big[F_v(k) + F_w(k)\big] \tag{8}$$

is the anisotropy residual of the tensor (Eqs. 23 and 26–27 of KL89): for isotropic turbulence $J \equiv 0$ and Eq. 7 reduces to its first (main) term, which is the form used in Goulart et al. (2011). Since the convective components have distinct variances and length scales, the initial turbulence is anisotropic and the corrections are not negligible: they act at the energy-containing scales—displacing the spectral peak towards lower wavenumbers—while leaving the inertial subrange intact. With the bilateral-to-unilateral convention factor of KL89 included, the construction closes the normalization automatically, $\int_0^\infty E_0\,dk = \frac{1}{2}\sum_j \sigma_j^2$, removing the amplitude rescaling required in Goulart et al. (2003, 2011). The components F_u, F_v and F_w entering Eqs. 7 and 8 are the one-dimensional components of the three-dimensional spectrum: the fractal (β-model) spectra of Goulart et al. (2024), generalized within the spectral family of KL89 through a transition-sharpness parameter μ_0,

$$F_j(k) = \frac{A_j}{\Big[1 + (B_j\,k)^{2\mu_0}\Big]^{\frac{p}{2\mu_0}}}, \qquad p = 8/3 - D, \qquad j = u, v, w, \tag{9}$$

where $D \le 1$ is the fractal dimension of the intermittent cascade and μ_0 the sharpness of the transition between the energy-containing range and the inertial subrange; the physical content of both parameters is developed in Sects. 3.2 and 3.3. For every (D, μ_0) the coefficients A_j and B_j preserve the component variances σ_j^2 and the spectral peaks $k_p = 2\pi(f_m)_j/z$ of the original fractal spectra, with $(f_m)_j$ the reduced frequencies of the peaks:

$$B_j = (p-1)^{-\frac{1}{2\mu_0}}\,\frac{z}{2\pi(f_m)_j}, \qquad A_j = \frac{2\mu_0\,\Gamma\Big(\dfrac{p}{2\mu_0}\Big)}{\Gamma\Big(\dfrac{1}{2\mu_0}\Big)\,\Gamma\Big(\dfrac{p-1}{2\mu_0}\Big)}\,\sigma_j^2\,B_j, \tag{10}$$

where Γ is the gamma function, so that $\int_0^\infty F_j\,dk = \sigma_j^2$ exactly, for every (D, μ_0); the complete derivation of Eqs. 9 and 10 is given in Appendix 1. The variances σ_j^2 are not obtained from the spectrum itself: they are external inputs, prescribed by the closed convective-similarity expression of Goulart et al. (2024) (their Eq. 27, obtained by integrating their fractal spectra),

$$\sigma_j^2 = C_j\Big(\frac{3}{5-3D}\Big)^p\,(2\pi)^{D-\frac{5}{3}}\,\Big(\frac{z}{z_i}\Big)^{2/3}\,z^{1-D}\,\big[(f_m)_j\big]^{D-\frac{5}{3}}\,\ell_j^{D-1}\,\psi_\varepsilon^{2/3}\,w_*^2, \tag{11}$$

with $C_u = 1/2$ and $C_v = C_w = 2/3$, where ℓ_j are the energy-containing length scales and $(f_m)_j$ the reduced peak frequencies of convective similarity (Degrazia et al. 2000),

$$
\begin{aligned}
(f_m)_u = (f_m)_v = \frac{z/z_i}{1.5}, \qquad (f_m)_w = \frac{z/z_i}{1.8\,\Phi}, \\
\ell_u = \ell_v = 0.21\, z_i \sqrt{\frac{0.01\, z_i}{|L|}}, \qquad \ell_w = 0.25\, z_i \sqrt{\frac{0.01\, z_i}{|L|}}\; \Phi,
\end{aligned}
\tag{12}
$$

where $\Phi = 1 - e^{-4z/z_i} - 0.0003\, e^{8z/z_i}$ and L is the Obukhov length. Equation 11 is the only place where the dissipation rate enters the initial components, through $\sigma_j^2 \propto \psi_\varepsilon^{2/3} w_*^2$: it sets the spectral energy level, while B_j sets the peak position and (D, μ_0) the shape. As μ_0 varies at fixed (σ_j^2, k_p), Eq. 9 merely redistributes the same variance in wavenumber (the inertial-range amplitude is renormalized accordingly by the Γ-factor of A_j; Appendix 1). For $\mu_0 = 1/2$, Eq. 9 recovers the fractal spectra of Goulart et al. (2024), with $A_j = (p-1)\,\sigma_j^2 B_j$: as shown in Appendix 1, Eqs. 9–11 with $\mu_0 = 1/2$ reproduce, term by term, the vertical spectrum of Eq. 25 of Goulart et al. (2024) expressed in wavenumber. The one-dimensional components of the decaying turbulence are related to the evolving three-dimensional spectrum through the weight-function relation of Goulart et al. (2007) (Eq. 24 of Goulart et al. 2011),

$$
F_i(k,t,z) = c(k)\, \frac{\dfrac{1}{T}\displaystyle\int_0^t F_i(k,t',z)\, dt'}{\dfrac{1}{T}\displaystyle\int_0^t E(k,t',z)\, dt'}\, E(k,t,z), \qquad i = u,v,w,
\tag{13}
$$

where the ratio between the two time integrals is a weight function that measures the contribution of the component i to the construction of the three-dimensional spectrum and $c(k)$ is a proportionality constant. In the present work this partition is generalized to a prognostic form in Sect. 3.5.

3.2 Fractal Generalization of the Inertial Transfer

The inertial-transfer closure of Pao, $v = \alpha^{-1}\varepsilon^{1/3}k^{5/3}$ (Sect. 3.1), assumes that the turbulent structures responsible for the spectral energy flux fill space homogeneously, which leads to the classical $k^{-5/3}$ stationary solution. The LES spectra of Darbieu et al. (2015), however, are systematically steeper than $-5/3$ under fully convective conditions (their Fig. 10b), a feature also reported by Lothon et al. (2009). We remove the space-filling assumption by writing the equilibrium spectrum of an intermittent (β-model) cascade whose active structures occupy, at each step, a fraction of space characterized by a dimension $D \leq 1$ (Frisch 1995; Goulart et al. 2022, 2024),

$$
E(k) = \alpha\, \varepsilon^{2/3}\, \ell_w^{D-1}\, k^{-(8/3-D)},
\tag{14}
$$

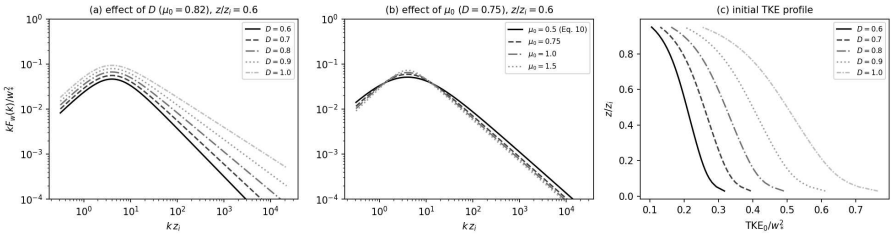


Fig. 1 Initial vertical fractal spectrum (Eq. 9): (a) pre-multiplied vertical spectrum $kF_w(k)$ at $0.6\,z_i$ for several values of D at fixed μ_0; (b) the same for several values of μ_0 at fixed D ($\mu_0 = 1/2$ recovers the fractal spectra of Goulart et al. 2024); (c) initial TKE profile for the same values of D (independent of μ_0). D controls the inertial slope and the total energy, μ_0 the sharpness of the peak at fixed variance; the TKE profile remains monotonic for every D

where ℓ_w is the energy-containing length scale of the vertical component and α the Kolmogorov constant. Requiring, as in the original argument of Pao (1965), that Eq. 14 be the constant-flux solution of the transfer term determines the high-wavenumber behaviour of the flux velocity uniquely,

$$v_{\mathrm{frac}}(k) = \alpha^{-1}\varepsilon^{1/3}\,\ell_w^{1-D}\,k^{8/3-D}, \tag{15}$$

which reduces to the Pao form for $D = 1$. In the present formulation Eq. 15 is the large-k limit of the stationary velocity of Eq. 3: since $E_0 \propto k^{-(8/3-D)}$ at high wavenumbers while Φ tends to a constant there, $v_{\mathrm{st}} \propto k^{8/3-D}$, so the cascade geometry (the exponent D) is inherited by the transfer exactly as in the closed-form fractal Pao closure.

The one-dimensional component spectra are those of Eqs. 9 and 10: their high-wavenumber exponent is the fractal one, $F_j \propto k^{-(8/3-D)}$, so the components and the cascade share the same dimension D. The parameter μ_0 plays, in the components, the same role as the sharpness μ in the KL89 fitting family—it controls the curvature of the transition between the energy-containing range and the inertial subrange—while D controls the inertial slope; the two are nearly orthogonal in the diagnostics, which is exploited in the calibration of Sect. 3.3. The initial condition is an exact stationary solution of the balance equation for all (D, μ_0). Figure 1 illustrates the two controls: D sets simultaneously the inertial slope and the total energy (a), μ_0 sets the sharpness of the spectral peak at fixed variance (b), and the initial TKE profile remains monotonic for every D (c). Note that the pre-multiplied inertial slope of Eq. 14 is $D - 5/3$: the fractal dimension is read from the observed inertial subrange, which is exploited in the next subsection.

3.3 Height-Dependent Profiles $D(z)$ and $\mu_0(z)$

The spectral slopes in the inertial subrange in the LES simulations by Darbieu et al. (2015) depend systematically on height, even during the quasi-stationary midday state (Fig. 10b of the paper): ranging from -0.9 to -1.0

(pre-multiplied values) in the 0.15–0.3 z_i range, versus -0.78 to -0.80 in the upper half of the CBL and ≈ -0.55 (the broad surface spectrum of Kaimal et al. 1972) near the ground. Classical spectral models, constructed based on surface-layer data, do not exhibit such variation. Darbieu et al. (2015) highlight the steep slopes in the intermediate region of the CBL and qualitatively attribute them to coherent structures, noting that this explanation "requires further study to be confirmed."

A height- and regime-dependent inertial slope is in fact consistent with a growing body of independent evidence. Caughey and Palmer (1979), combining the Ashchurch and Minnesota data, documented a systematic change of the spectral shape through the depth of the CBL and a marked steepening above it. From Doppler-lidar measurements of vertical velocity through the CBL, Lothon et al. (2009) found spectra whose sharpness generally decreases with height in the lower CBL, inertial-subrange slopes "significantly steeper" than $-2/3$ in several of their cases, and steeper spectra precisely in the most convective conditions; in the seven-year Doppler-lidar climatology of Williams and Qiu (2022), the inertial-subrange slope steepens systematically as the energy in the production subrange (0.1–10 z_i) increases, i.e. with the transition to narrow, intense buoyant updrafts. Charrondière and Stiperski (2024) showed that the departures of unstable surface-layer spectra from the classical scaled shapes are organized by the local turbulence anisotropy. Deviations of inertial-range scaling from Kolmogorov similarity connected to intermittency are likewise well documented in the atmospheric boundary layer, through the scaling exponents of the velocity structure functions and their dependence on stratification (Vindel and Yagüe 2011), the clusterization intermittency of high-frequency wind records (Liu and Hu 2020), and direct estimates of the fractal dimension of the velocity components and of its dependence on stability (Tijera et al. 2016). The height-dependent slopes of the BLLAST LES thus join a consistent picture: the inertial subrange of convective boundary-layer turbulence is not universally $-5/3$, and its slope carries information about the spatial organization of the cascade.

In light of Eq. 14, the slope profile translates into a dimension profile, and the profile of the μ plateau into a sharpness profile. The two static profiles are calibrated jointly, level by level, on the two digitized diagnostic sets of the LES: the midday inertial slopes (their Fig. 10b) constrain D, and the afternoon μ plateaus (their Fig. 12) constrain μ_0. The two controls are nearly orthogonal—the local sensitivities are $\partial(\text{slope})/\partial D \simeq 1.0$, $\partial(\text{slope})/\partial\mu_0 \simeq -0.1$, $\partial\mu/\partial D \simeq -2.6$ and $\partial\mu/\partial\mu_0 \simeq +1.2$—so the 2×2 calibration is well posed, constraining the anchors to about ± 0.03 in D and ± 0.1 in μ_0. The resulting anchor points (z/z_i; D; μ_0) are (0.05; 0.81; 0.50), (0.15; 0.68; 0.68), (0.30; 0.60; 0.71), (0.50; 0.78; 0.88), (0.60; 0.75; 0.82), (0.75; 0.61; 0.57) and (0.90; 0.62; 0.57), with linear interpolation (Fig. 2a) and two active floors ($\mu_0 \geq 1/2$ at the surface; $D \geq 0.60$ at 0.3 z_i). The profile is markedly intermittent at every level ($D = 0.60$–0.81): most space-filling near the surface, where shear-driven turbulence dominates; most intermittent at 0.3 z_i, where coherent thermals concentrate the active cascade in a small fraction of space;

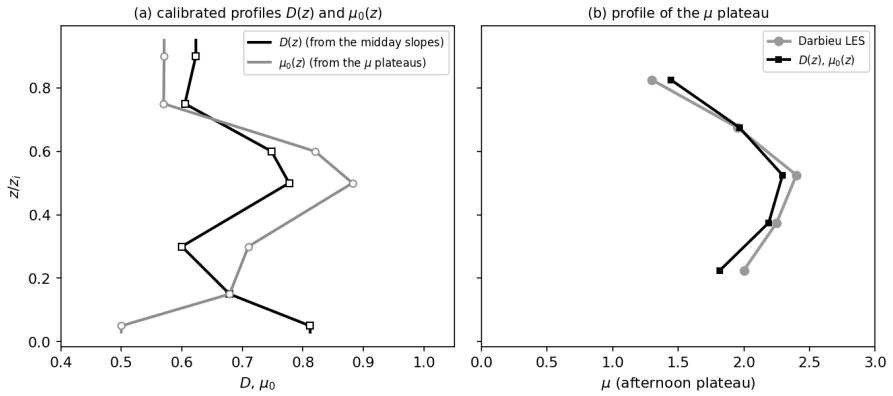


Fig. 2 (a) Static calibrated profiles $D(z)$ (black; from the digitized midday slopes) and $\mu_0(z)$ (grey; from the digitized μ plateaus); symbols mark the anchor points. (b) Vertical profile of the μ plateau: LES (digitized) and model with the calibrated profiles. The calibrated profiles reproduce the magnitude and the shape of the LES profile, with its maximum at 0.45–0.6 z_i

and intermittent again in the entrainment-affected upper CBL, where the LES combines a broad peak with a relatively steep tail (Sect. 5.2). The sharpness μ_0 peaks in the mid-CBL and falls to the broad Kaimal limit ($\mu_0 = 1/2$) at the surface. This reading gives quantitative content to the qualitative attribution of the steep slopes to coherent structures by Darbieu et al. (2015).

Because the profiles are static, they preserve every invariance of the model: the initial TKE profile remains monotonic, the surface spectra remain unchanged throughout the transition, and the closure quantities (c_1, C_R and the stationary transfer velocity itself) are still fixed by the $t = 0$ balance with no empirical adjustment ($C_R = 1.8$–3.5 above $0.3\,z_i$, the classical Rotta range). One point must be stated plainly: with $\mu_0(z)$ calibrated on the LES plateaus, the plateau *value* of μ is partly prescribed rather than predicted. The predictive content of the model resides in the temporal behaviour—the stability of the plateau through the afternoon, the timing and shape of its collapse, and the slope flattening—and in the vertical structure of the transition. The intermittent geometry characterizes the whole afternoon, and the late-afternoon signature comes from the forcing shut-off over that fixed geometry (Sect. 4.4).

3.4 Time Structure of the Forcing During the Transition

Two extensions of Goulart et al. (2011) describe the forcing decay. First, the mechanical term also weakens, $M(k,t,z) = M_0(k,z)\,S(t)$ with $S(t) = u_*^2(t)/u_*^2(0)$, following the slower observed decay of u_* in BLLAST (from 0.2 to $0.1\,\mathrm{m\,s^{-1}}$). Second, the thermal source is decomposed according to the physical origin of the linear buoyancy-flux profile, and each component is given its

own shut-off law,

$$S_H(t,z) = (1-\hat{z})\,T - 0.2\,\hat{z}\,T^{\lambda} + g(\hat{z})\,T^{\gamma}, \qquad T(t) = \cos\!\Big(\frac{\pi}{2}\frac{t}{\tau_f}\Big), \tag{16}$$

where $\hat{z} = z/z_i$, $g(\hat{z}) = 0.3\max\big[0,\,(\hat{z}-0.4)/0.6\big]$ is the turbulent-transport gain that feeds the upper half of the CBL (Moeng and Sullivan 1994), and $\lambda = \gamma = 2$ are the shut-off exponents of the entrainment and penetrative-transport components. The three terms are the locally surface-driven flux, the entrainment flux and the penetrative transport. The hierarchy is physical: the penetrative transport is the product of the thermal mass flux ($\propto T$) and of the fraction of thermals that still reach the upper CBL ($\propto T$), hence T^2; the entrainment flux, driven by the weakening convection, follows the same quadratic law; the locally surface-driven part persists as T. At $t = 0$ the bracket reduces to the Moeng–Sullivan profile $(1 - 1.2\hat{z}) + g(\hat{z})$ (Moeng and Sullivan 1994), so the initial state and all closures are strictly unaffected; $\lambda = \gamma = 1$ recovers the uniform shut-off of Goulart et al. (2011).

The uniform shut-off has a structural defect exposed by the absolute-rate onset criterion of Darbieu et al. (2015): since the initial TKE decreases with height, a height-uniform relative forcing decay makes the top start decaying last—the opposite of the observations. A quasi-stationary argument makes this precise: while the decay is slow, $\mathrm{TKE}_{\mathrm{eq}} \propto S_H^{2/3}$, so the absolute rate $\propto \mathrm{TKE}_0\,|dS_H/dt|$ crosses the criterion threshold first where TKE_0 is largest. The quadratic laws accelerate $|dS_H/dt|$ in the upper CBL without ever making the forcing negative before τ_f, and remove the inversion: t_{TKE} becomes nearly uniform at 13.3–14.2 UTC across 0.2–0.9 z_i, against the observed slight decrease from 13.1 to 12.5 UTC, while the relative TKE evolution remains as close to the LES as with uniform forcing (Fig. 3). The residual +0.6–1.1 h onset delay, and the fact that in this family of laws an earlier onset can only be bought at the price of an excessive amplitude decay at the top, are discussed in Sect. 5.2.

3.5 Prognostic Spectral Partition

The diagnostics of Darbieu et al. (2015) concern the vertical-velocity spectrum F_w, not the total E. In Goulart et al. (2007, 2011) the component spectra were obtained from E by fixed weight functions, which freezes the anisotropy at its initial value. Here the method is generalized: the fractions $R_i(k,t) = F_i/E$ ($i = u, v, w$) become prognostic,

$$\frac{\partial R_i}{\partial t} = \frac{S_i - R_i S_E}{E} - \frac{C_R}{\tau(k)}\Big[R_i - \hat{R}_i(k)\Big], \qquad \tau(k) = \varepsilon^{-1/3}k^{-2/3}, \tag{17}$$

where S_i is the source of component i—buoyancy feeds $\overline{w'w'}$ ($S_w = 2S_H$-weighted), shear feeds $\overline{u'u'}$, and $S_v = 0$—S_E is the source of the E equation, and the second term is a return-to-isotropy relaxation of Rotta type acting on

the eddy-turnover time $\tau(k)$: fast at high wavenumbers (local isotropy), slow at low wavenumbers (anisotropy persists in the large scales). The closure follows the same philosophy as c_1 and the stationary transfer velocity: the level-wise scalar C_R and the target partition $\hat{R}_i(k)$ are determined by requiring exact stationarity of Eq. 17 at $t = 0$, with C_R the smallest value ($\geq$1.8) for which $\hat{R}_w > 0$ at all k. No empirical anisotropy constant is introduced; that the procedure returns $C_R = 1.8$–3.5 above $0.3\,z_i$—the classical range of the Rotta constant—is a nontrivial consistency check. The target $\hat{R}_i$ absorbs the physics not explicitly represented (wall blocking, one- to three-dimensional aliasing, pressure covariances) and is the state towards which the partition relaxes when the forcing shuts off. The fixed-partition method is recovered as the limiting case of Eq. 17 with frozen fractions. At the lowest level ($0.05\,z_i$) the procedure degenerates ($C_R \sim 10^2$): the partition is anchored by the wall, which is the physically correct limit but outside the useful range of the closure.

3.6 Why the Budget Terms Control the Inertial-Subrange Slope

The qualitative mechanism can be stated in three steps. (i) In the fully convective regime, the buoyant and mechanical sources, Eqs. 4 and 5, inject energy with the distributed spectral weight $k^{-2/3}E_0$, which reaches the low-wavenumber edge of the inertial subrange; a source acting inside the subrange steepens and sharpens the local equilibrium beyond the pure-cascade shape. The steeper-than-Kolmogorov midday slopes are therefore a joint signature of the intermittent cascade (Sect. 3.2) and of the distributed forcing. (ii) While the forcing decays slowly ($\tau_f \gg t_*$), the spectrum tracks a sequence of quasi-equilibria in which the weight of the distributed source decreases towards zero, and the equilibrium shape relaxes accordingly—flatter and broader, since the term that steepened and sharpened it is being withdrawn. The flattening is thus the spectral signature of the *progressive* removal of the distributed source—a budget effect, formalizing hypothesis (b) of Darbieu et al. (2015)—and does not require any change of the cascade geometry or of the anisotropy. It is specific to the slow-transition regime: a sudden removal of the source throws the spectrum into free decay, which narrows it instead (Sect. 4.4). (iii) The vertical structure follows from the ratio of mechanical to thermal production, $M/H \sim (u_*^3/\kappa z)/(w_*^3/z_i)$: below $|L|$ the mechanical term, which persists into the evening, dominates and freezes the spectral shape—the surface invariance—while aloft the decay is purely convective and the spectrum responds to the shut-off.

4 Results

4.1 Turbulence Kinetic Energy Decay and Onset Times

Figure 3a compares the evolution of relative TKE obtained with the spectral model (Eq. 1) against digitized LES curves at three heights. The model re-

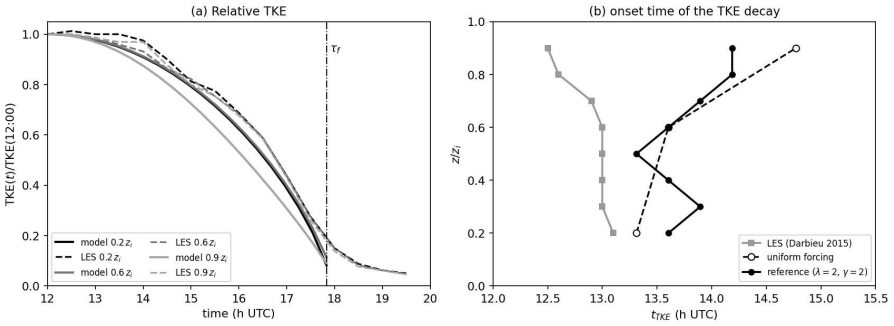


Fig. 3 (a) Evolution of relative TKE at 0.2, 0.6 and $0.9\,z_i$: spectral model (solid lines) compared to the LES of Darbieu et al. (2015) (dashed lines; curves digitized from Fig. 7 of that study). The vertical line indicates the zero-crossing point of the surface buoyancy flux (τ_f, 1750 UTC). Note the two-phase decay and the near-homogeneity of the relative decay with respect to height. Model curves are drawn up to τ_f, beyond which the convective model is outside its domain of validity (Sect. 5.2). (b) Onset time of TKE decay (absolute rate criterion of Darbieu et al. 2015): LES (grey squares), model with uniform forcing shut-off (dashed; note the spurious inversion with respect to height), and spectral model with $\lambda = \gamma = 2$ (black)

produces the two-phase decay—slow until $\sim 0.75\,\tau_f$, with TKE $\approx 0.55\,\mathrm{TKE}_0$ at the inflection point, and rapid thereafter, reaching 8–11% of the midday value at τ_f at all levels—as well as the near-vertical homogeneity of the relative decay, with amplitudes at 1500 UTC of 0.81 and 0.74 at 0.6 and $0.9\,z_i$, compared to 0.80 and 0.68 in the LES. Near the surface, TKE is maintained after τ_f by persistent mechanical production, as observed. Beyond τ_f the convective model leaves its domain of validity—the developing residual layer is wave-dominated (Sect. 5.2)—and the model curves are therefore drawn up to the buoyancy-flux reversal only.

Figure 3b shows the onset time of the TKE decay by the absolute-rate criterion. The uniform shut-off produces the spurious inversion anticipated in Sect. 3.4 (t_{TKE} increasing from 13.3 to 14.8 UTC between 0.2 and $0.9\,z_i$); the component-wise forcing removes it, giving a nearly uniform profile at 13.3–14.2 UTC against the observed 12.5–13.1 UTC. The residual uniform delay of +0.6–1.1 h is discussed in Sect. 5.2.

4.2 Evolution of the Vertical-Velocity Spectra

Figure 4 compares the vertical velocity spectra modeled at a height of $0.6\,z_i$ at 1500 UTC (mid-afternoon, quasi-stationary phase) and at 1750 UTC (the buoyancy-flux reversal, end of the convective phase) directly with the LES of Darbieu et al. (2015); the LES curves are reconstructed from the fit that those authors applied to their spectra (the form of Kristensen et al. 1989), using the digitized parameters μ and l_w of the 0.45–$0.6\,z_i$ slice (nearest available times 1500 and 1730). At 1500 UTC the two spectra agree closely over the whole

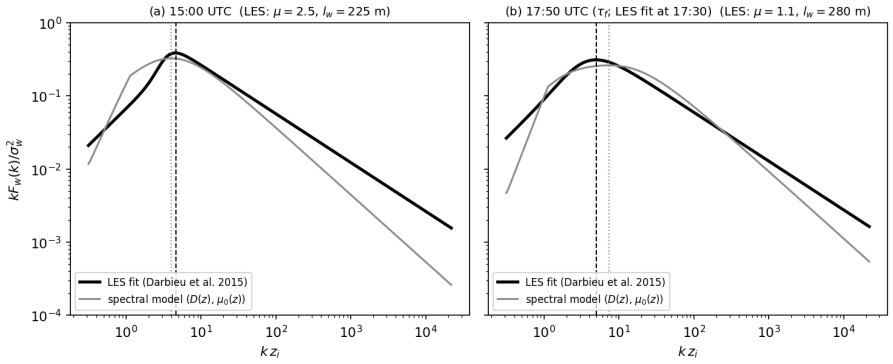


Fig. 4 Vertical-velocity spectra at $0.6\,z_i$ at (a) 1500 UTC and (b) 1750 UTC (τ_f): spectral model (grey) against the LES of Darbieu et al. (2015) (black; curves reconstructed from the fit applied by those authors to the LES spectra, with the digitized parameters μ and l_w of the 0.45–0.6 z_i slice; nearest available fit times 1500 and 1730). Both curves are normalized by the variance. The dashed and dotted vertical lines mark the spectral peaks of the LES and of the model, respectively

resolved range: the energy-containing peaks nearly coincide ($\Lambda_w \simeq 1.6\,z_i$ in the model against $1.4\,z_i$ in the LES)—a direct consequence of the anisotropy corrections of Eq. 7, which add energy at low wavenumbers—and the model follows the LES through the resolved inertial subrange (a fit of the same form to the model curve gives $\mu = 2.3$, against the LES value of 2.5 at this slice; cf. Table 1). At the flux reversal the LES spectrum has flattened dramatically ($\mu = 1.1$ at 1730, reaching 0.6 by 1800) while keeping its energy at large scales. The model reproduces the flattening with comparable amplitude—its fitted sharpness drops from 2.3 to 1.4—but its peak migrates to somewhat smaller scales ($\Lambda_w \simeq 0.85\,z_i$ against $\sim$1.3 z_i in the LES), so part of the low-wavenumber side of the broadening is underestimated. This is the spectral counterpart of the residual lag of the μ collapse discussed in Sect. 4.3. Beyond τ_f the modelled spectrum leaves the convective regime and the KL89 diagnostics cease to be meaningful (Sect. 5.2), which is why the comparison is closed at the reversal.

4.3 Sharpness Parameter and Inertial Slope

Figures 5 and 6 overlay the model on the digitized LES curves of $\mu(t)$ (Fig. 12 of Darbieu et al. 2015) and of the pre-multiplied inertial slope (their Fig. 10b), slice by slice; Table 1 summarizes the plateau values. With the calibrated profiles the plateau magnitude and vertical shape are both reproduced (Table 1; Fig. 2b): 1.82–2.29 below $0.75\,z_i$ against the observed 2.0–2.4, 1.44 at the top against 1.30, with the maximum at the observed height. The plateau values are, by construction, partly calibrated (Sect. 3.3); what is not imposed is their *stability*: the fitted μ holds constant through five afternoon hours, while the TKE decays by half, because the quasi-stationary balance protects the spectral shape (Fig. 5). The midday slopes follow the LES closely: -0.79 at 0.45–0.6 z_i

Table 1 Plateau values of μ and midday pre-multiplied inertial slopes by height slice: digitized LES targets (Darbieu et al. 2015) against the model with the calibrated static profiles $D(z)$, $\mu_0(z)$. Digitization uncertainty ± 0.2

	μ plateau		Inertial slope of kF_w $(t = 0)$	
Slice	LES	$D(z), \mu_0(z)$	LES	$D(z), \mu_0(z)$
0.15–$0.3\,z_i$	2.00	1.82	-0.95	-0.84
0.3–$0.45\,z_i$	2.25	2.19	—	-0.85
0.45–$0.6\,z_i$	2.40	2.29	-0.80	-0.79
0.6–$0.75\,z_i$	1.95	1.97	—	-0.79
0.75–$0.9\,z_i$	1.30	1.44	-0.78	-0.77
Surface	0.45	0.66	-0.58	-0.59

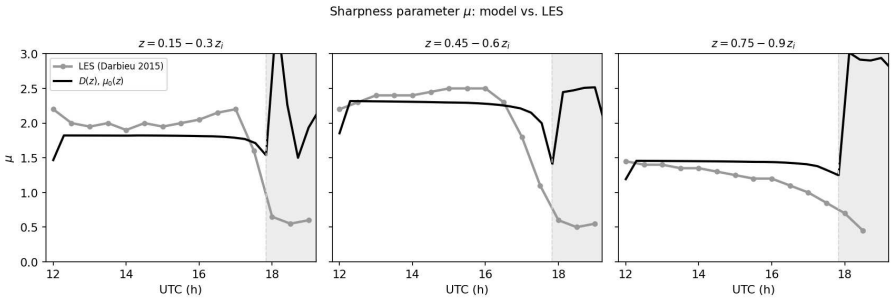


Fig. 5 Sharpness parameter $\mu(t)$ by height slice: digitized LES (grey; Fig. 12 of Darbieu et al. 2015) and model with the calibrated profiles $D(z)$, $\mu_0(z)$ (black). The shaded window $(t > \tau_f)$ lies outside the domain of validity of the convective spectrum: there the fitted μ of the model rebounds spuriously (Sect. 5.2)

and -0.77 at 0.75–$0.9\,z_i$ against the observed -0.80 and -0.78, while at 0.15–$0.3\,z_i$ the profile closes most of the distance towards the steep observed -0.95 (-0.84, limited by the $D \geq 0.60$ floor). The surface is invariant through the forced phase ($\mu = 0.66 \pm 0.01$ and slope -0.59 ± 0.01 until $\sim$1630 UTC, against the observed 0.45 and -0.58).

The late collapse of μ begins after 1700 UTC and reaches 1.4 at τ_f at mid-CBL. In the LES the collapse begins near 1630 and reaches 1.1 by 1730 and 0.6 by 1800: the modelled collapse is therefore shallower within the convective window and lags by about half an hour. Immediately after τ_f the modelled spectrum leaves the convective regime and its fitted μ rebounds spuriously (grey window in Fig. 5); the post-τ_f window is excluded from the comparison (Sect. 5.2).

4.4 Attribution: Which Terms Produce the Flattening

To identify the mechanisms that produce the flattening, four switch-on/switch-off numerical experiments were performed at $0.6\,z_i$ with the reference configuration, all starting from the same stationary initial state and differing only

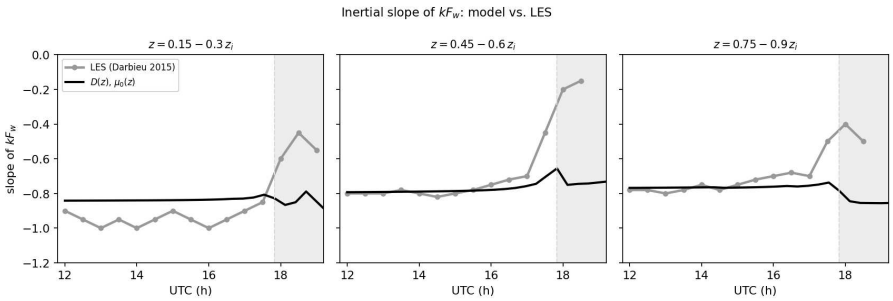


Fig. 6 Pre-multiplied inertial slope of kF_w by height slice: digitized LES (grey; Fig. 10b of Darbieu et al. 2015) and model with the calibrated profiles $D(z)$, $\mu_0(z)$ (black). At 0.45–0.6 and 0.75–0.9 z_i the model coincides with the LES; at 0.15–0.3 z_i the profiles close most of the distance to the steep observed slopes. The shaded window ($t > \tau_f$) is outside the domain of validity of the convective spectrum (Sect. 5.2)

in the time structure of the forcing: a *Control* run, with the progressive cosine shut-off of Sect. 3.4; a *Frozen* run, in which the thermal source is held at its midday value, $(g/T_0)H(k,t,z) = (g/T_0)H(k,0,z)$, everything else as in the Control; a *NoM* run ("no mechanical production"), with the shear term of Eq. 5 switched off, $M = 0$, everything else as in the Control; and a *Sudden* run, with a step shut-off of both sources at $t = 0$, $M = (g/T_0)H = 0$—free decay in the sense of Nieuwstadt and Brost (1986). Figure 7 shows the outcome of each experiment individually, as the variance-normalized pre-multiplied vertical-velocity spectrum at three times of the afternoon.

The experiments identify the mechanism, and sharpen it. In the Control run (Fig. 7a) the pre-multiplied slope holds -0.80 until ≈1630 UTC and flattens to -0.66 at τ_f, with the fitted μ collapsing from 2.3 to 1.4: the flattening emerges late and gently, and is strongest in the mid and upper CBL—exactly the BLLAST phenomenology. The Frozen run (Fig. 7b) shows no flattening at any time (the slope is constant to within 0.01 over six hours): the signature belongs to the shut-off, not to any slow internal drift of the model. The NoM run (Fig. 7c) is indistinguishable from the Control above the surface layer in this weak-wind case ($|L| \approx 6$ m): shear protects the spectral shape only very close to the ground, which is precisely why the surface spectra are invariant. The Sudden run (Fig. 7d) is the instructive counterpoint: the spectrum does *not* flatten—it narrows, the energy-containing range draining within about one convective turnover time and the spectral peak migrating by two decades towards high wavenumbers (the fitted length scale collapses from ∼400 to ∼6 m while the inertial slope never flattens), the same behaviour the model exhibits after τ_f (Sect. 5.2). The narrowing is consistent with the sudden shut-off LES of Tkachenko et al. (2022), in which a fast-decay interval of duration $\sim t_*$ drains the vertical-velocity spectrum over its whole wavenumber range—by an order of magnitude—rather than flattening it. The flattening is therefore not a property of free decay: it is the signature of the *progressive* shut-off, during which the spectrum tracks a sequence of quasi-equilibria

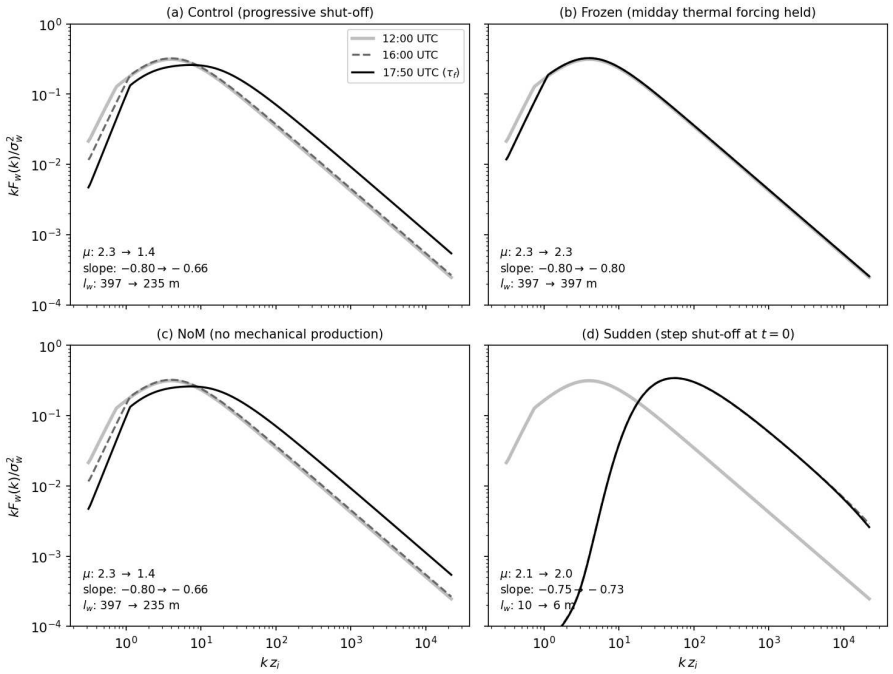


Fig. 7 Switch-on/switch-off experiments at $0.6\,z_i$ (reference configuration): variance-normalized pre-multiplied vertical-velocity spectra $kF_w(k)/\sigma_w^2$ at 1200 UTC (thick grey), 1600 UTC (dashed) and 1750 UTC (τ_f; black), for (a) the Control run (progressive cosine shut-off), (b) the Frozen run (thermal source held at its midday value), (c) the NoM run (no mechanical production) and (d) the Sudden run (step shut-off of both sources at $t = 0$). Annotations give the fitted μ, the pre-multiplied inertial slope and the fitted length scale l_w, from the early-afternoon plateau to τ_f. Only the progressive shut-off (a, c) flattens the spectrum; the Frozen run is invariant, and in the Sudden run the free decay completes within about one convective turnover time—the 1600 and 1750 curves coincide—narrowing the spectrum instead of flattening it

whose distributed buoyant source—the term that steepens and sharpens the forced spectrum (Sect. 3.6)—is withdrawn gradually. Once the source is gone, the pure-cascade dynamics narrows the spectrum again. The slope flattening observed during the transition is thus a forced-relaxation effect, possible only in the slow-transition regime $\tau_f \gg t_*$, which is precisely the regime of the BLLAST afternoon.

Together with Sect. 4.3, this establishes the central result: the flattening of the inertial-subrange slope and the collapse of μ are the spectral-budget signature of the progressive removal of the distributed buoyant source acting over a fixed intermittent cascade geometry. No change of the cascade efficiency and no change of the anisotropy are required.

4.5 Anisotropy

Figure 8 shows the anisotropy of the modelled turbulence in the form used by Darbieu et al. (2015) (their Fig. 9b): vertical profiles of the ratio $(\sigma_u^2 + \sigma_v^2)/2\sigma_w^2$ at selected times of the convective window (a) and its time evolution at three levels (b). The prognostic partition, Eq. 17, lets the anisotropy evolve independently of the spectral shape, and its evolution reproduces the observed pattern. During the forced phase the CBL interior is w-dominated, with $(\sigma_u^2 + \sigma_v^2)/2\sigma_w^2 \simeq 0.8$–$0.9$ in the mid-CBL and $\simeq 2.3$ near the surface (the "squashed" surface eddies), and the profiles are nearly invariant from 1300 to 1700 UTC (the three forced-phase curves of Fig. 8a are indistinguishable); the vertical anisotropy σ_w^2/σ_u^2 at $0.6\,z_i$ increases from 1.35 at noon to $\simeq 1.44$ through the afternoon (the "more anisotropy" noted by Darbieu et al.). Only in the last half hour before the reversal does the partition begin to collapse towards a w-deficient state, the ratio rising through 1.2–1.3 at τ_f at all levels above $0.15\,z_i$: the onset of the return-to-isotropy destruction of the w excess as its asymmetric (buoyant) source disappears. Continued past the reversal, this collapse leads towards the pancake-like residual turbulence, consistent with the increase of anisotropy during the decay found by Pino et al. (2006) and with the sequence documented by Tkachenko et al. (2022)—isotropization during the fast-decay interval, followed by growing anisotropy and the formation of a quasi-two-dimensional, horizontally dominated flow—although the post-τ_f window itself is outside the scope of the analysis (Sect. 5.2). Without the Rotta relaxation (source term only) the anisotropy diverges; with it, the emergent C_R values sit in the classical range. Figure 8b makes the timing explicit: the anisotropy transition is locked to τ_f, after the μ collapse has begun. The model thus discriminates the two hypotheses of Darbieu et al. (2015)—the spectral flattening (their "cascade" hypothesis, made quantitative here as a budget effect) does not require the anisotropy change, which evolves by a separate mechanism (asymmetric forcing plus return-to-isotropy) on its own schedule.

5 Discussion

5.1 Physical Interpretation

The picture that emerges is economical. During the afternoon the CBL spectrum is held in a forced quasi-equilibrium whose shape—steeper than Kolmogorov, with a μ plateau whose vertical profile mirrors $D(z)$ and $\mu_0(z)$—is set jointly by the intermittent cascade geometry and by the distributed buoyant source. The intermittency is a property of the convective regime itself, present at every level ($D = 0.60$–0.81): weakest near the surface, where shear-driven turbulence is closest to space-filling, strongest at $0.3\,z_i$, where coherent thermals concentrate the active turbulence in a small fraction of space, and strong again in the entrainment-affected upper CBL, where intermittent engulfment shapes the spectra. This reading gives quantitative content to the

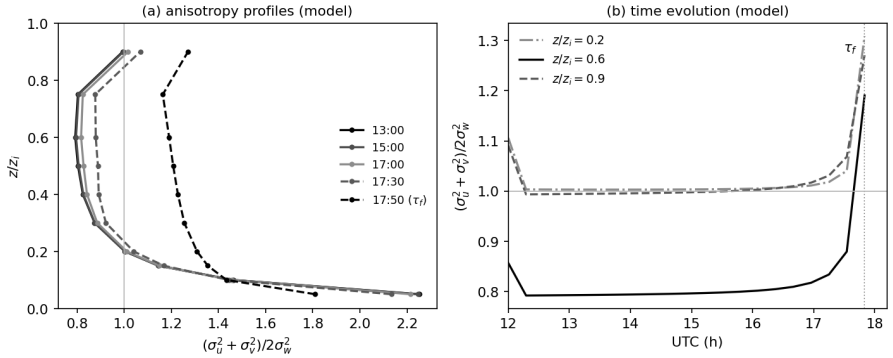


Fig. 8 Anisotropy of the modelled turbulence (reference run), in the form of Fig. 9b of Darbieu et al. (2015): (a) vertical profiles of $(\sigma_u^2 + \sigma_v^2)/2\sigma_w^2$ at selected times of the convective window (solid lines: forced phase; dashed: last half hour before the reversal); (b) time evolution of the same ratio at three levels, up to the buoyancy-flux reversal (dotted vertical line: τ_f). The forced-phase profiles (1300–1700 UTC) are nearly indistinguishable: the anisotropy is quasi-invariant through the afternoon, and the collapse towards a w-deficient state begins only at the shut-off

qualitative attribution of the steep slopes to coherent structures by Darbieu et al. (2015), and it rests on an observation that has received little systematic attention—the height dependence of the inertial slope in the quasi-stationary CBL, absent from classical surface-based spectral models—although it is consistent with a body of independent evidence reviewed in Sect. 3.3 (Caughey and Palmer 1979; Lothon et al. 2009; Vindel and Yagüe 2011; Tijera et al. 2016; Liu and Hu 2020; Williams and Qiu 2022).

The late-afternoon signature then requires no new physics: as the distributed source is progressively withdrawn, the spectrum tracks a sequence of quasi-equilibria of decreasing source weight, and the KL89 fit registers this forced relaxation as a simultaneous flattening and broadening (μ collapse)—hypothesis (b) of Darbieu et al. (2015) made quantitative, with two amendments: the cascade itself does not change (what changes is the balance in which it sits), and the flattening is specific to the slow shut-off—in free decay, after a sudden removal of the source, the spectrum narrows instead (Sect. 4.4). The forced-relaxation reading finds independent support in the free-convective LES of El Guernaoui et al. (2019), in which the variance-normalized vertical-velocity spectrum flattens and broadens through the transition—explicitly in line with Darbieu et al. (2015)—and, within the inertial subrange, the largest scales are the most affected by the decay, as expected if the withdrawn source acts at the low-wavenumber edge of the subrange. The anisotropy, meanwhile, evolves on its own schedule (asymmetric forcing during the afternoon, return-to-isotropy collapse at the shut-off), so the spectral transition neither requires nor is driven by the anisotropy transition—discriminating the two candidate explanations that the LES alone could not separate. The model further predicts that the spectral broadening is transient, ending with the heat flux: a

testable statement. The surface invariance follows from the production ratio M/H (Sect. 3.6): in this weak-wind case the mechanical term dominates only below $|L| \sim 6$ m, yet its persistence into the evening anchors the near-surface spectrum—and the near-surface $\mu \simeq 0.5$ plateau of the observations is the Kaimal broad-spectrum limit (Kaimal et al. 1972; Kaimal 1978), which the model reproduces as $\mu_0 = 1/2$ with the mechanical anchor.

On the cascade side, the relation to Moeng and Wyngaard (1988) deserves note: their "more efficient cascade in free decay" is, in the present budget, amended—the change of spectral shape does not come from the decay itself (in free decay the modelled spectrum narrows, Sect. 4.4) but from the progressive weakening of the distributed source that had steepened and sharpened the forced equilibrium: efficiency does not increase; the forcing that shaped the equilibrium disappears slowly enough for the spectrum to follow. And the β-model generalization connects the CBL literature to the intermittency literature (Frisch 1995; Vindel and Yagüe 2011; Tijera et al. 2016; Goulart et al. 2022): the estimate $0.60 \leq D \leq 0.81$, obtained here from the joint calibration on two nearly orthogonal diagnostics of a boundary-layer LES, falls at the lower edge of the range quoted for fully developed convective turbulence—convective boundary-layer turbulence is, in this reading, substantially more intermittent than homogeneous-flow estimates suggest.

5.2 Limitations

Five limitations of the present version are declared explicitly. (L1) The post-τ_f window is outside the domain of validity of the convective model, which is why the analysis is closed at the buoyancy-flux reversal. After the reversal the transfer term of Eq. 2, linear in E for any flux velocity, drains the energy-containing range on the convective turnover time: the modelled TKE falls below 1% of its midday value within 1.5 h of the shut-off, while the LES keeps a residual 10–20% for hours around 1830 UTC, with l_w growing from $\sim$200 to $\sim$1000 m (Fig. 11 of Darbieu et al. 2015). The modelled spectrum also narrows—its peak migrates towards high wavenumbers as the energy-containing range drains—and the fitted KL89 parameters rebound spuriously (μ rises to 2.5–3, while the LES stays broad, $\mu \to 0.55$). The physical reason is that the residual layer is no longer decaying convective turbulence: as it becomes weakly stably stratified, eddies larger than the Ozmidov scale (Ozmidov 1965) turn into gravity waves and stop cascading—a scale-selective arrest of the spectral transfer that the convective spectral families of KL89 and Goulart et al. (2007, 2011) do not contain and cannot fit. The quasi-two-dimensional reorganization of the residual flow found in the LES of Tkachenko et al. (2022), with its markedly reduced dissipation relative to the isotropic state, points in the same direction. The post-τ_f diagnostics are therefore reported as out of scope; the core results of the paper concern $t \leq \tau_f$, and the residual layer is left for future work (Sect. 6). Related to this, within the convective window the final collapse of μ is shallower than observed (1.4 at τ_f against 1.1 at 1730

in the LES) and lags by about half an hour. (L2) In the T^λ/T^γ family of shut-off laws, onset time and amplitude at the top trade off along a Pareto frontier: a sustained forcing deficit advances the onset but depresses the amplitude (quasi-stationarily, $\mathrm{TKE}_{\mathrm{eq}} \propto S_H^{2/3}$), and the LES combination—onset at 12.5 UTC with near-homogeneous amplitude—lies outside the reachable set. The reference $\lambda = \gamma = 2$ eliminates the onset inversion and matches the amplitudes; a residual +0.6–1.1 h delay remains. (L3) The model contains no nocturnal stable-boundary-layer physics: after τ_f the near-surface layer should evolve into a shallow stable boundary layer with shrinking scales, a regime outside the scope of the model. (L4) The fitted length scale of the diurnal plateau is too large: $l_w \simeq$ 380–470 m against 165–245 m in the LES (a factor $\sim$2). The anisotropy corrections of Eq. 7, which bring the spectral peak onto the LES one (Fig. 4a), also inflate the integral scale returned by the KL89 fit; the relative growth of l_w across the transition, not its absolute value, is the meaningful diagnostic. (L5) In the entrainment zone (0.75–0.9 z_i) the LES exhibits a broad peak and a relatively steep tail, a combination that strains the KL89 functional family: with the calibrated profiles the model settles at $\mu = 1.44$ against the observed 1.30, at the price of low D and μ_0 values there, whose physical reading (strong intermittency in the entrainment zone) remains to be confirmed independently.

Beyond these, the general limitations of the approach are those of its parentage (Goulart et al. 2003, 2011): heuristic (though initially-balanced) closures, horizontal homogeneity, no coupling with the heat equation, and Monin–Obukhov similarity applied to a decaying late-afternoon surface layer at the edge of its validity. In addition, with $\mu_0(z)$ calibrated on the LES plateaus, the plateau values of μ are partly prescribed (Sect. 3.3); the temporal and vertical structure of the transition remains the predictive content. The digitization of the LES targets adds $\pm$0.2 uncertainty to the ordinates, comparable to the effect of the $\pm$0.03 anchor uncertainty of $D(z)$ and $\pm$0.1 of $\mu_0(z)$.

6 Conclusions

The spectral TKE-budget model of Goulart et al. (2003, 2011), extended with an initial spectrum built from the complete (anisotropic) spectral velocity tensor of Kristensen et al. (1989) and made an exact stationary solution of the discrete balance, an intermittent cascade of height-dependent fractal dimension with a height-dependent component sharpness, and a component-wise decay law for the thermal forcing, reproduces the essential spectral phenomenology of the BLLAST afternoon transition documented by Darbieu et al. (2015): the two-phase, nearly height-homogeneous TKE decay; the μ plateau with the observed magnitude and vertical shape, its stability through the afternoon, and its collapse in the last hour before the buoyancy-flux reversal; the flattening of the inertial-subrange slope at the right time; and the invariance of the near-surface spectra.

The central answer to the question posed by Darbieu et al. (2015) is that the flattening and the μ collapse are the spectral-budget signature of the *progressive* shut-off of the distributed buoyant source over a fixed intermittent cascade geometry. Neither a change of cascade efficiency nor an anisotropy transition is required; the latter occurs, but by a separate mechanism and on a separate schedule. The mechanism is specific to the slow-transition regime: in the model, a sudden shut-off narrows the spectrum instead of flattening it, so the observed flattening is a signature of forcing that decays slowly relative to the convective turnover time—precisely the BLLAST regime. The near-surface invariance follows from the persistence of mechanical production, and the model predicts—testably—that the spectral broadening is transient, ending with the heat flux.

Two by-products may have interest beyond the transition problem. First, the height dependence of the quasi-stationary inertial slope in the CBL, read from the LES of Darbieu et al. (2015) and consistent with independent observational evidence (Sect. 3.3), yields through the β-model a static dimension profile $D(z) = 0.60$–0.81: convective boundary-layer turbulence is markedly intermittent at every level, most strongly where coherent thermals and entrainment organize the flow. Second, the closure strategy—the transfer velocity and every constant, including the Rotta-type relaxation coefficient of the prognostic spectral partition, fixed by exact stationarity of the initial balance—returned the Rotta constant in its classical range without any empirical input, and eliminated both the amplitude rescaling of the initial spectrum and the separate high-wavenumber (Frisch) closure constant of Goulart et al. (2003, 2011).

In future work, we intend to perform the quantitative comparison with other BLLAST intensive observation periods using observed (rather than perturbed) parameters; to extend the model beyond the buoyancy-flux reversal into the residual layer, where the spectral transfer must be arrested selectively at scales larger than the Ozmidov scale (Ozmidov 1965) of the developing stratification (made prognostic by coupling the spectral budget with a heat-transfer equation) and where the convective spectral family must be replaced by one suited to the wave-dominated regime (including the post-shut-off narrowing of the modelled spectrum, Sect. 5.2); to derive the $D(z)$ and $\mu_0(z)$ profiles dynamically from the statistics of coherent structures; and to employ the decaying spectra obtained here in the derivation of eddy diffusivities for dispersion models in the late-afternoon transition (Goulart et al. 2007, 2024; Goulart 2026; Koleva and Vulkov 2023).

Acknowledgements This work was supported in part by CNPq and CAPES, Brazilian funding agencies.

Declarations

Funding This work was supported in part by CNPq and CAPES, Brazilian funding agencies.

Conflict of interest The authors declare no competing interests.

Availability of data and materials The large-eddy simulation and observational targets used in this work were digitized from the published figures of Darbieu et al. (2015), and the BLLAST data are available as described in Lothon et al. (2014).

Appendix 1: Derivation of the Generalized Component Spectra, Eqs. 9 and 10

A1.1 The Spectral Family and the Two Constraints

The starting point is the fitting family with which KL89 represent measured one-dimensional spectra (their Eq. 53): a form that is finite and flat at $k \to 0$, decays as $k^{-5/3}$ at $k \to \infty$, is four times differentiable (a requirement of the tensor construction of Eq. 7), and whose curvature in the transition between the energy-containing range and the inertial subrange is controlled by a sharpness parameter μ. The generalization adopted here keeps the family but replaces the Kolmogorov asymptotic exponent 5/3 by the fractal one, $p = 8/3 - D$:

$$F_j(k) = \frac{A_j}{\left[1 + (B_j k)^{2\mu_0}\right]^{p/(2\mu_0)}}, \qquad j = u, v, w. \tag{18}$$

Indeed, for $k \to \infty$,

$$F_j(k) \;\longrightarrow\; A_j B_j^{-p}\, k^{-p} \;\propto\; k^{-(8/3-D)}, \tag{19}$$

so the components and the cascade share the same dimension D, while $F_j(0) = A_j$ is finite, as in the spectra of Goulart et al. (2024) (their Eq. 26). The two constants per component are fixed by requiring that, *for every* (D, μ_0), the family preserve the two observable invariants of the original fractal spectra: the peak of the pre-multiplied spectrum at $k_p = 2\pi(f_m)_j/z$, and the variance σ_j^2 of Eq. 11. Without these constraints, varying μ_0 would change the energy and displace the peak, and the effects of D and μ_0 on the diagnostics would cease to be nearly orthogonal (Sect. 3.3).

A1.2 B_j from the Pre-multiplied Peak

The peak of $kF_j(k)$ satisfies $F_j + kF_j' = 0$. Differentiating Eq. 18,

$$F_j'(k) = -\,p\,A_j\,B_j^{2\mu_0} k^{2\mu_0 - 1} \left[1 + (B_j k)^{2\mu_0}\right]^{-p/(2\mu_0)-1}, \tag{20}$$

so that

$$F_j + kF_j' = F_j(k)\left[1 - \frac{p\,(B_j k)^{2\mu_0}}{1+(B_j k)^{2\mu_0}}\right] = 0 \quad \Longrightarrow \quad (B_j k_p)^{2\mu_0} = \frac{1}{p-1}, \tag{21}$$

which gives the first part of Eq. 10,

$$B_j = (p-1)^{-\frac{1}{2\mu_0}}\,\frac{z}{2\pi (f_m)_j}. \tag{22}$$

The factor $(p-1)^{-1/(2\mu_0)}$ cancels the μ_0-dependence of the peak position exactly: the pre-multiplied maximum sits at k_p for every (D, μ_0).

A1.3 A_j from the Variance

Imposing $\int_0^\infty F_j\,dk = \sigma_j^2$ with the substitution $u = (B_j k)^{2\mu_0}$, $dk = u^{\frac{1}{2\mu_0}-1}du/(2\mu_0 B_j)$,

$$\int_0^\infty F_j\,dk = \frac{A_j}{2\mu_0 B_j}\int_0^\infty \frac{u^{\frac{1}{2\mu_0}-1}}{(1+u)^{\frac{p}{2\mu_0}}}\,du = \frac{A_j}{2\mu_0 B_j}\,\mathrm{B}\Big(\frac{1}{2\mu_0},\,\frac{p-1}{2\mu_0}\Big), \tag{23}$$

by the Euler representation of the Beta function, $\int_0^\infty u^{x-1}(1+u)^{-(x+y)}du = \Gamma(x)\Gamma(y)/\Gamma(x+y)$ with $x = 1/(2\mu_0)$ and $y = (p-1)/(2\mu_0)$ (convergent for $p > 1$, $\mu_0 > 0$). Solving for A_j gives the second part of Eq. 10. Because this normalization holds identically in (D, μ_0), the variance returned by integrating Eq. 9 is, by construction, the input σ_j^2 of Eq. 11: prescribing the variance by the similarity expression of Goulart et al. (2024)—the integral of the $\mu_0 = 1/2$ member—introduces no inconsistency for $\mu_0 \neq 1/2$. What changes with μ_0 at fixed (σ_j^2, k_p) is only the distribution of that variance in wavenumber: from Eq. 19, the coefficient of the inertial tail,

$$A_j B_j^{-p} = \frac{2\mu_0\,\Gamma\big(\frac{p}{2\mu_0}\big)}{\Gamma\big(\frac{1}{2\mu_0}\big)\Gamma\big(\frac{p-1}{2\mu_0}\big)}\,(p-1)^{\frac{p-1}{2\mu_0}}\,\sigma_j^2\,k_p^{p-1}, \tag{24}$$

decreases as the transition sharpens (e.g., to 0.73 of its $\mu_0 = 1/2$ value at $\mu_0 = 0.82$, $D = 0.75$): a sharper peak concentrates energy near k_p, and the effective fractal constant of the k^{-p} range is renormalized accordingly.

A1.4 Reduction to the Spectra of Goulart et al. (2024) at $\mu_0 = 1/2$

For $\mu_0 = 1/2$, Eqs. 9 and 10 reduce, using $\Gamma(p) = (p-1)\Gamma(p-1)$ and $p - 1 = (5-3D)/3$, to

$$F_j(k) = \frac{A_j}{(1+B_j k)^p}, \qquad B_j = \frac{3}{5-3D}\,\frac{z}{2\pi (f_m)_j}, \qquad A_j = (p-1)\,\sigma_j^2 B_j. \tag{25}$$

The vertical spectrum of Goulart et al. (2024) (their Eq. 25) is written in reduced frequency $f = nz/u$; with Taylor's hypothesis, $k = 2\pi n/u$ and $F_w(k)\,dk =$

$S_w(n)\,dn$ give $f = kz/2\pi$ and the identity of the pre-multiplied spectra, $kF_w(k) = nS_w(n)$. From Eq. 25,

$$B_w k = \frac{3}{5-3D}\,\frac{f}{(f_m)_w}, \qquad A_w k = (p-1)\,\sigma_w^2\,B_w k = \sigma_w^2\,\frac{f}{(f_m)_w}, \tag{26}$$

since $(p-1)\cdot 3/(5-3D) = 1$, so that

$$\frac{kF_w(k)}{w_*^2} = \frac{\sigma_w^2}{w_*^2}\,\frac{f/(f_m)_w}{\Big[1+\dfrac{3}{5-3D}\,\dfrac{f}{(f_m)_w}\Big]^{8/3-D}}. \tag{27}$$

Substituting σ_w^2 from Eq. 11 yields, term by term, Eq. 25 of Goulart et al. (2024):

$$\frac{nS_w(n)}{w_*^2} = \frac{\Big(\dfrac{3}{5-3D}\Big)^{\frac{8}{3}-D}(2\pi)^{D-\frac{5}{3}}\,C_w\,\ell_w^{D-1}\,\Big(\dfrac{z}{z_i}\Big)^{\frac{2}{3}}\,z^{1-D}\,\psi_\varepsilon^{\frac{2}{3}}\,f}{\big[(f_m)_w\big]^{\frac{8}{3}-D}\Big[1+\dfrac{3}{5-3D}\,\dfrac{f}{(f_m)_w}\Big]^{\frac{8}{3}-D}}, \tag{28}$$

and the corresponding relations hold for the u and v components with their scales and constants of Eqs. 11 and 12.

References

Caughey SJ, Palmer SG (1979) Some aspects of turbulence structure through the depth of the convective boundary layer. Q J R Meteorol Soc 105:811–827

Charrondière C, Stiperski I (2024) Spectral scaling of unstably stratified atmospheric flows: turbulence anisotropy and the low-frequency spread. Q J R Meteorol Soc 150:4196–4216

Darbieu C, Lohou F, Lothon M, Vilà-Guerau de Arellano J, Couvreux F, Durand P, Pino D, Patton EG, Nilsson E, Blay-Carreras E, Gioli B (2015) Turbulence vertical structure of the boundary layer during the afternoon transition. Atmos Chem Phys 15:10,071–10,086

Degrazia GA, Anfossi D, Carvalho JC, Mangia C, Tirabassi T, Campos Velho HF (2000) Turbulence parameterisation for PBL dispersion models in all stability conditions. Atmos Environ 34:3575–3583

El Guernaoui O, Reuder J, Esau I, Wolf T, Maronga B (2019) Scaling the decay of turbulence kinetic energy in the free-convective boundary layer. Boundary-Layer Meteorol 173:79–97

Frisch U (1995) Turbulence: The Legacy of A. N. Kolmogorov. Cambridge University Press, Cambridge

Goulart A (2026) A model for the decay of TKE in the CBL from the time evolution of the length and velocity scales: application in a Eulerian dispersion model. Environ Fluid Mech

Goulart A, Degrazia G, Rizza U, Anfossi D (2003) A theoretical model for the study of convective turbulence decay and comparison with large-eddy simulation data. Boundary-Layer Meteorol 107:143–155

Goulart A, Suarez JMS, Lazo MJ (2022) Modelling fractal turbulent velocity spectra: application to a dispersion model of contaminants in particular cases of the planetary boundary layer. Boundary-Layer Meteorol 183:407–421

Goulart A, Suarez JMS, Lazo MJ, Marques JC (2024) Evaluation of the eddy diffusivity in a pollutant dispersion model in the planetary boundary layer. Environ Fluid Mech 24:489–504

Goulart AG, Vilhena MT, Degrazia GA, Flores DT (2007) Vertical, lateral and longitudinal eddy diffusivities for a decaying turbulence in the convective boundary layer. Ecol Model 204:516–522

Goulart AG, Bodmann BEJ, de Vilhena MTMB, Soares PMM, Moreira DM (2011) On the time evolution of the turbulent kinetic energy spectrum for decaying turbulence in the convective boundary layer. Boundary-Layer Meteorol 138:61–75

Grant ALM (1997) An observational study of the evening transition boundary-layer. Q J R Meteorol Soc 123:657–677

Grimsdell AW, Angevine WM (2002) Observations of the afternoon transition of the convective boundary layer. J Appl Meteorol 41:3–11

Kaimal JC (1978) Horizontal velocity spectra in an unstable surface layer. J Atmos Sci 35:18–24

Kaimal JC, Wyngaard JC, Izumi Y, Coté OR (1972) Spectral characteristics of surface-layer turbulence. Q J R Meteorol Soc 98:563–589

Koleva MN, Vulkov LG (2023) Numerical solution of fractional models of dispersion contaminants in the planetary boundary layer. Mathematics 11:2040

Kristensen L, Lenschow DH, Kirkegaard P, Courtney M (1989) The spectral velocity tensor for homogeneous boundary-layer turbulence. Boundary-Layer Meteorol 47:149–193

Liu L, Hu F (2020) Finescale clusterization intermittency of turbulence in the atmospheric boundary layer. J Atmos Sci 77:2375–2392

Lothon M, Lenschow DH, Mayor SD (2009) Doppler lidar measurements of vertical velocity spectra in the convective planetary boundary layer. Boundary-Layer Meteorol 132:205–226

Lothon M, Lohou F, Pino D, Couvreux F, Pardyjak ER, Reuder J, Vilà-Guerau de Arellano J, Durand P, et al. (2014) The BLLAST field experiment: Boundary-Layer Late Afternoon and Sunset Turbulence. Atmos Chem Phys 14:10,931–10,960

Moeng CH, Sullivan PP (1994) A comparison of shear- and buoyancy-driven planetary boundary layer flows. J Atmos Sci 51:999–1022

Moeng CH, Wyngaard JC (1988) Spectral analysis of large-eddy simulations of the convective boundary layer. J Atmos Sci 45:3573–3587

Nadeau DF, Pardyjak ER, Higgins CW, Fernando HJS, Parlange MB (2011) A simple model for the afternoon and early evening decay of convective turbulence over different land surfaces. Boundary-Layer Meteorol 141:301–324

Nieuwstadt FTM, Brost RA (1986) The decay of convective turbulence. J Atmos Sci 43:532–546

878 Ozmidov RV (1965) On the turbulent exchange in a stably stratified ocean.
879 Izv Atmos Ocean Phys 1:861–871
880 Pao YH (1965) Structure of turbulent velocity and scalar fields at large
881 wavenumbers. Phys Fluids 8:1063–1075
882 Park SB, Baik JJ, Han BS (2020) Role of wind shear in the decay of convective
883 boundary layers. Atmosphere 11:622
884 Pino D, Jonker HJJ, Vilà-Guerau de Arellano J, Dosio A (2006) Role of shear
885 and the inversion strength during sunset turbulence over land: characteristic
886 length scales. Boundary-Layer Meteorol 121:537–556
887 Rizza U, Miglietta MM, Degrazia GA, Acevedo OC, Anfossi D (2013) Sunset
888 decay of the convective turbulence with large-eddy simulation under realistic
889 conditions. Physica A Stat Mech Appl 392:4481–4490
890 Sorbjan Z (1997) Decay of convective turbulence revisited. Boundary-Layer
891 Meteorol 82:503–517
892 Tijera M, Maqueda G, Yagüe C (2016) Influence of atmospheric stratification
893 on the integral scale and fractal dimension of turbulent flows. Nonlin Process
894 Geophys 23:407–417
895 Tkachenko EV, Debolskiy AV, Mortikov EV (2021) Intercomparison of subgrid
896 scale models in large-eddy simulation of sunset atmospheric boundary layer
897 turbulence: computational aspects. Lobachevskii J Math 42:1580–1595
898 Tkachenko EV, Debolskiy AV, Mortikov EV, Glazunov AV (2022) Large-eddy
899 simulation and parameterization of decaying turbulence in the evening tran-
900 sition of the atmospheric boundary layer. Izv Atmos Ocean Phys 58:219–236
901 Vindel JM, Yagüe C (2011) Intermittency of turbulence in the atmospheric
902 boundary layer: scaling exponents and stratification influence. Boundary-
903 Layer Meteorol 140:73–85
904 Williams IN, Qiu S (2022) Long-term observations of turbulence vertical veloc-
905 ity spectra in a convective mixed layer: dependence on land-surface forcing in
906 the U.S. Southern Great Plains. J Geophys Res Atmos 127:e2022JD037,137